Modeling of a superconducting sensor with microring-embedded gold-island space–time control

M. Bunruangses, A. E. Arumona, P. Youplao, N. Pornsuwancharoen, K. Ray & P. Yupapin

Journal of Computational Electronics

ISSN 1569-8025

J Comput Electron
DOI 10.1007/s10825-020-01548-9

Springer

Journal of Computational Electronics
https://doi.org/10.1007/s10825-020-01548-9

Modeling of a superconducting sensor with microring-embedded gold-island space–time control

M. Bunruangses[1] · A. E. Arumona[2,3,4] · P. Youplao[5] · N. Pornsuwancharoen[5] · K. Ray[6] · P. Yupapin[2,3]

Abstract
A superconducting sensing circuit using silicon microring-embedded gold-island space–time control is proposed for a low-current source sensor. Feeding an optical field centered at a wavelength of 1.50 μm into the circuit with suitable parameters results in the formation of a whispering-gallery mode. The electric field is the space source, being multiplexed in time to construct the space–time function. Space–time control is achieved using two side phase modulators to obtain a path difference between the polaritons (trapped electrons) at resonance. The space and time uncertainty saturate simultaneously due to the nonlinear Kerr effect. The polariton oscillation obeys a two-level system in which the oscillation time collapses at resonance. The oscillation signal is recognized as the Rabi oscillation, which enables the operation of the circuit under forward- or reverse-biased directional switching. The results of this work show that the current of the proposed circuit increases exponentially in both the forward- and reverse-bias directions. The switching time of the Rabi oscillation is 1.50 μs, while the current–voltage characteristic of the circuit exhibits sensitivity values ranging from 0.82 to 1.90 μA nV^{-1}. This performance confirms that the microring circuit can be used as a superconducting sensing circuit for low-current sensor applications.

Keywords Relativistic electronics · Superconducting sensor · Microring circuit · Current sensor

1 Introduction

Superconducting materials exhibit superconductivity, where the corresponding physical property (electrical resistance) reduces to zero. Various types of superconductor are known, being classified according to their response to a (electric or magnetic) field, mode of operation, temperature response, and type of material [1]. Superconductor sensors show a response to small changes in their electrical environment. Superconductors have been used in different applications by many researchers. Sadleir et al. [2] developed a model for transition-edge sensors made from superconducting materials. They investigated the response of the sensors to a magnetic field, obtaining results that were in good agreement

✉ P. Yupapin
preecha.yupapin@tdtu.edu.vn

M. Bunruangses
montree.b@rmutp.ac.th

A. E. Arumona
arumonaarumonaedward.st@student.tdtu.edu.vn

P. Youplao
phichai.po@rmuti.ac.th

N. Pornsuwancharoen
nithiroth.po@rmuti.ac.th

K. Ray
kanadray00@gmail.com

[1] Department of Computer Engineering, Faculty of Industrial Education, Rajamangala University of Technology Phra Nakhon, Bangkok 10300, Thailand

[2] Computational Optics Research Group, Advanced Institute of Materials Science, Ton Duc Thang University, District 7, Ho Chi Minh City, Vietnam

[3] Faculty of Applied Sciences, Ton Duc Thang University, District 7, Ho Chi Minh City, Vietnam

[4] Division of Computational Physics, Institute for Computational Science, Ton Duc Thang University, Ho Chi Minh City 700000, Vietnam

[5] Department of Electrical Engineering, Faculty of Industry and Technology, Rajamangala University of Technology Isan Sakon Nakhon Campus, Sakon Nakhon 47160, Thailand

[6] Amity School of Applied Sciences, Amity University Rajasthan, Jaipur, India

Published online: 22 July 2020

with other studies. Chen et al. [3] investigated the thermal response of a transition-edge sensor designed in the form of a superconducting circuit, developing a thermal model and applying it to analyze the thermal response of the superconducting sensor circuit. Kvitkovic et al. [4] studied the magnetic field response of a high-temperature superconductor. Their study involved both experimental work and numerical simulations. The result revealed a significant response of the superconductor sensor to a magnetic field. Wang et al. [5] developed a model to analyze the transition temperature of a superconductor transition-edge sensor. Their analysis of the model provided results that were in good agreement with other studies. Kunniyoor et al. [6] studied superconducting sensors and developed a model for their characterization. The model was used to analyze the thermal response of the superconductor sensors, providing results that were in good agreement with experimental results. Wang et al. [7] designed and developed a superconducting sensor circuit and modeled it based on two-fluid theory. The superconducting circuit consisted of a transition-edge sensor, and the results of the analysis were in good agreement with those of other studies. Holdengreber et al. [8] designed and developed a bow-tie antenna for a superconductor sensor based on a Josephson junction. Their study involved both experimental work and numerical simulations, revealing an impressive response of the Josephson junction to an impedance mismatch. The numerical simulation results were also in good agreement with the experimental results. Shibata et al. [9] designed and fabricated a superconducting sensor in the form of a nanostrip. They investigated the photoresponse of the sensor, finding that it was applicable as a photon detector. Sun et al. [10] developed a novel high-temperature superconductor resonator in the form of a microstrip in which a whispering-gallery mode with a high Q-factor was formed. Kato et al. [11] studied the power-handling ability of a superconductor filter comprising a disk and ring resonators. They also investigated how the power-handling ability of the superconductor filters could be improved. Sekiya et al. [12] developed a new design for a high-temperature superconductor resonator for use in high-power applications. Their double-strip superconductor resonator was fabricated using an electromagnetic simulator and investigated for use at high powers. Pi et al. [13] studied the current distribution of a hybrid design comprising both low- and high-temperature superconductors. The current distribution was measured both experimentally and numerically. The results revealed that the current was transferred from the low- to high-temperature superconductor, enabling its use in large-scale magnets. Xang et al. [14] developed a direct-current circuit breaker comprising current-limiting and interrupting parts. Superconductor tapes were used as the main components of the current-limiting part, with a resistance in parallel. The circuit breaker makes use of the superconductor to limit the current in the circuit consisting of current-limiting and interrupting parts. Superconductor tapes were used as the main components in the current limiting part, with a resistance in parallel. The circuit breaker makes use of a superconductor to limit the current in the circuit. Zhu et al. [15] studied the current distribution of a high-temperature superconductor cable, where a novel measurement method was developed and applied to determine the current distribution, alternating-current loss, and cable critical current. Li et al. [16] improved the distribution of the electric field in high-temperature superconductor cable terminals by using epoxy–ZnO composites with a nonlinear conductivity response. The nonlinearity increased the strength of the electric field distribution in the high-temperature superconductor. In the work presented herein, a superconducting circuit is modified by using microring-embedded gold islands to enable space–time distortion control. This work focuses on the response of the microring circuit to an external electric current with the aim of developing a low-current source sensor. A microring circuit consisting of an embedded gold thin film is proposed. When using suitable parameter values, resonant space–time distortion is obtained when the Rabi oscillation collapses. Circuit switching can be achieved using the superconducting sensor. Optiwave finite-difference time-domain (FDTD) software is first employed to determine the electric field distribution of the microring circuit and the formation of the whispering-gallery mode (WGM) [17]. MATLAB software is then employed in a second step, using the parameter values extracted from the results of the Optiwave FDTD simulations. Superconducting sensing is exhibited by the microring circuit using the space–time distortion control as simulated by MATLAB.

2 Theoretical background

The input is light with an electric field of [18]

$$E_{\text{in}} = E_0 \cdot \exp\left(-\mathrm{i}k_z z\right), \tag{1}$$

where the wavenumber is defined as $k_z = \frac{2\pi}{\lambda}$, the initial amplitude of the field is E_0, the propagation distance is z, and λ is the wavelength of the input field.

The space–time function is given by

$$E_{\text{add}} = D\mathrm{e}^{\pm \mathrm{i}2\pi\left(\frac{v}{\lambda}\right)\cdot t}, \tag{2}$$

where t is the time, v is the speed of light propagation in the medium, and D is the amplitude. The "±" sign indicates the full-time slot axis. The nonlinear effect known as the Kerr effect is described as $n = n_0 + n_2 I = n_0 + n_2 P/A_{\text{eff}}$, where n_0 and n_2 are the linear and nonlinear refractive indices,

respectively. I is the optical intensity, P is the optical power, and A_{eff} is the effective core area of the waveguide.

The Drude model [19] describes the behavior of electrons in a gold thin film, being expressed as

$$\epsilon(\omega) = 1 - \frac{ne^2}{\epsilon_0 m\omega^2}, \tag{3}$$

where ϵ_0 is the relative permittivity. The electron density, charge, and mass are denoted as n, e, and m, respectively. ω is the angular frequency. At resonance, the angular frequency becomes the plasma frequency, given as

$$\omega_{\text{p}} = \left[\frac{ne^2}{\epsilon_0 m}\right]^{-1/2} \tag{4}$$

From Eq. (4), the electron density is $n = \frac{\omega_{\text{p}}^2}{e^2}\epsilon_0 m$. The output fields of the structure are described as follows [20]:

$$E_{\text{th}} = m_2 E_{\text{in}} + m_3 E_{\text{ad}}, \tag{5}$$

$$E_{\text{dr}} = m_5 E_{\text{ad}} + m_6 E_{\text{in}}, \tag{6}$$

where the terms in Eqs. (5) and (6) are given in Ref. [20].

As shown in Fig. 1b, a current sensing environment is applied to the device close to the island region, which is the sensing transducer. Besides, remote sensing can also be achieved by applying a radiative electrical field to the circuit. Finally, the circuit is similar to a room-temperature superconducting circuit, as explained below. By using the kinetic equation applied for polaritons, the resonance condition for the polariton oscillation is expressed as $\sum_{i=1}^{n} \frac{1}{2} m_i v_i^2 = NK_{\text{B}}\Delta T$ [21], where m_i is the polariton mass, v_i is the polariton velocity, $N \approx 6 \times 10^{23}$ is Avogadro's number, K_{B} is the Boltzmann constant, and T is absolute temperature. When $\Delta t \to 0$, then $v^2 \to 0$, thus $\Delta T \to 0$, which is the superconducting circuit condition. This is, of course, suitable for low-current sensing applications.

3 Results and discussion

The structure of the microring circuit is shown in Fig. 1, including two linear waveguides, the silicon microring at the center ring with two small rings along the sides of the center ring, and a gold thin film (island) embedded at the center ring on the silicon substrate. Plasmons in the WGM cavities can form a sensing transducer when strong fields are introduced into the WGM cavities. The typical gap from the waveguide to the center ring (R_{D}) is 0.2 μm, where the Q-factor of a microring on a similar scale has been investigated and confirmed by various works [22]. For this work, the optimum results are obtained for a radius of 2.2 μm. The radius is varied from 0.2 to 2.8 μm, as presented in Table 1.

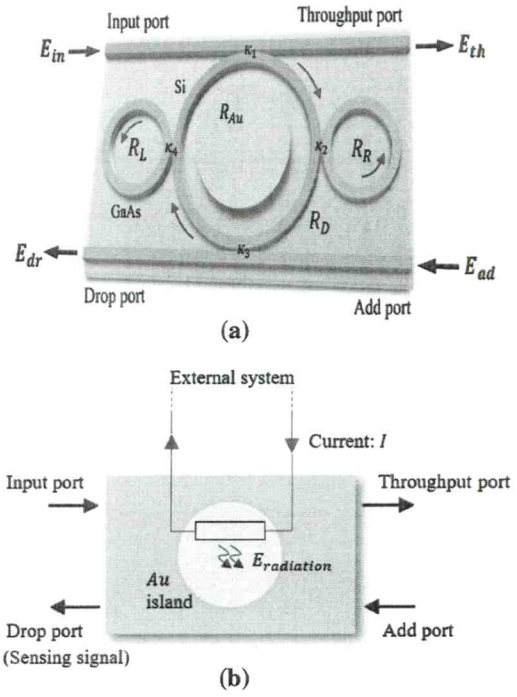

Fig. 1 A microring circuit with a gold thin film embedded at the center ring, where R_{L}, R_{R}, and R_{D} are the radius of the left, right, and center ring, respectively. The coupling coefficients are $\kappa_{\text{s}} = 0.5$. R_{Au} is the radius of the gold plate. E_{in}, E_{th}, E_{dr}, and, and E_{ad} represent the electrical fields at the input port, throughput port, drop port, and add port, respectively. **a** The circuit structure. **b** The sensing diagram

Table 1 The parameter values selected for the simulations [26, 27]

Parameter	Symbol	Value	Units
Input light power	P	100–500	mW
Gold plate radius	R_{Au}	0.2–2.8	μm
Gold plate thickness	T_{Au}	0.1–7.5	μm
Ring resonator radius	R_{s}	3.0	μm
Gold conductivity	σ	4.11×10^7	Sm^{-1}
Gold resistivity	ρ	2.44×10^{-8}	Ωm
Coupling coefficient	κ	0.50	
Insertion loss	γ	0.50	dB
Au refractive index	n	1.80	
Si refractive index	n_{Si}	3.42	
Si nonlinear refractive index	n_2	1.3×10^{-13}	$\text{m}^2\ \text{W}^{-1}$
Optical center wavelength	λ	1.55	μm
Plasma frequency	ω_{p}	1.299×10^{16}	rad s^{-1}
Core effective area	A_{eff}	0.30	μm^2
Free-space permittivity	ϵ_{o}	8.85×10^{-12}	F m^{-1}
Electron mass	m	9.11×10^{-31}	kg
Electron charge	e	1.60×10^{-19}	Coulomb
Waveguide loss	α	0.50	dB (mm)^{-1}

The input light with a center wavelength of 1.50 μm is fed into the system via the input port. When the input light illuminates the gold thin film at the center ring, electrons in the film are excited, resulting in the formation of the electron densities described by Eqs. (3) and (4). The two small rings act as phase modulators, inducing the nonlinear effect and coupling with the center ring. The parameter values selected for the simulations are presented in Table 1. The optimum whispering-gallery mode forms as the result of the nonlinear effect in the proposed circuit at the resonance of the center ring (Fig. 2). This can be used to trap electrons on the island surface. To simulate the interaction of the electric field in the microring circuit and the whispering-gallery mode, the 32-bit version 12.0 [23] of the Optiwave FDTD software is first employed. The simulation model has grid size of 0.07 and a mesh of 19,434,222 cells along three axes, x, y, and z, respectively. In the simulations, an anisotropic perfect matched layer with 15 layers and a theoretical reflection coefficient of 1.0×10^{-12} and 1.0 real tensor are employed as the boundary conditions. To confirm the results at resonance, 20,000 round trips are employed. MATLAB software is employed in the second step, using the parameter values extracted from the results of the Optiwave simulations. MATLAB is applied to simulate the electric field distribution in the presence of the superconductivity phenomenon. The input electric field is described by Eq. (1), being fed into the system described by Eqs. (5) and (6). Figure 3a shows the electric field distribution of the trapped electrons within the microring circuit. Figure 3b, c shows plots of the first output at the throughput port, the second output at the drop port, and the WGM in the wavelength and frequency domain, respectively. The electric field is the input space–time signal applied at the add port. The space source is multiplexed in time as described by Eq. (2), thereby constructing the input space–time function. Figure 4 shows a plot of the current

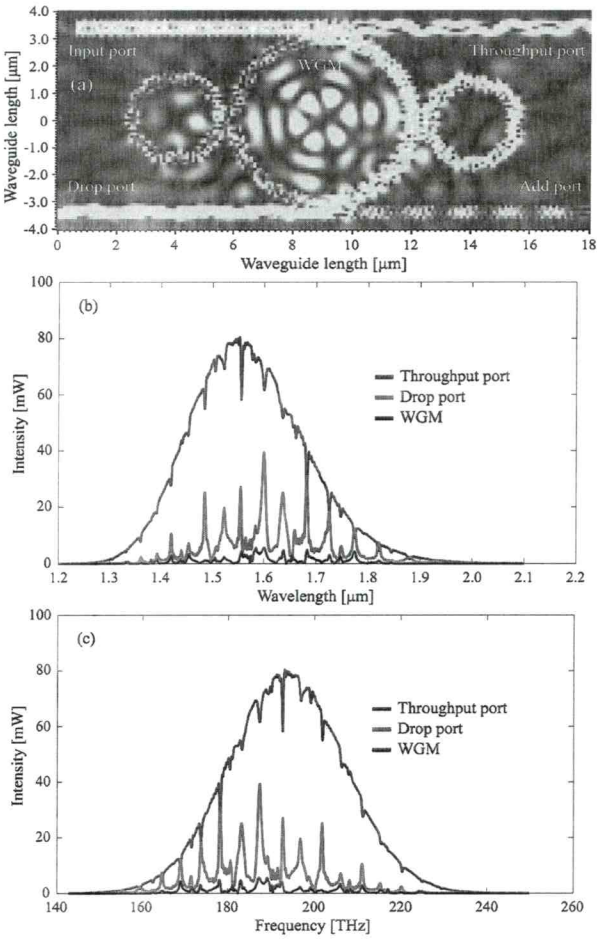

Fig. 3 Plots of the **a** electric field distribution of the circuit, and the results at the throughput port, drop port, and WGM in the **b** wavelength and **c** frequency domains obtained based on the Optiwave results shown in Fig. 2

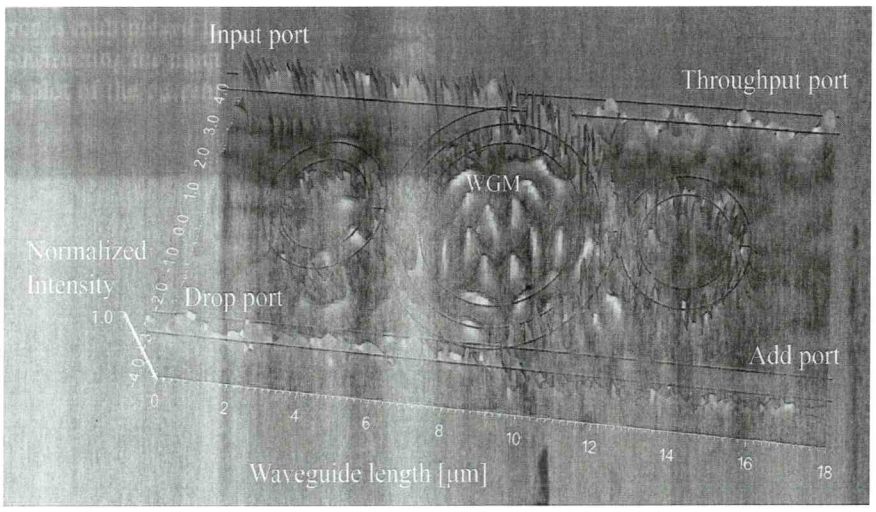

Fig. 2 The Optiwave results, showing the formation of the whispering-gallery mode. The ring system is described by $R_L = 1.50$ μm, $R_R = 1.49$ μm, $R_D = 3.0$ μm, $\kappa_1 = \kappa_2 = \kappa_3 = \kappa_4 = 0.5$, and $R_{Au} = 2.2$ μm, with a thickness of 0.2 μm and a height of 0.5 μm above the base, and $n_{Si} = 3.47$. The input power is 100 mW with a center wavelength of 1.55 μm, while the values for the other parameters are presented in Table 1

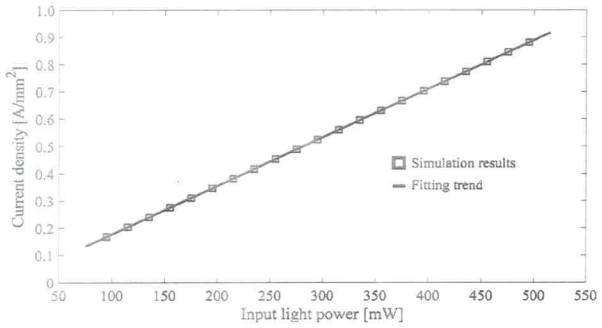

Fig. 4 The current density in the gold plate as a function of the input light power, where the gold plate has a radius of $R_{Au} = 2.2\,\mu m$ and a thickness of 200 nm

density, which can be considered as a function of the electric field inside the Au plate, thus providing a measure of the charge flowing through the Au plate. The current density is calculated as $n = \frac{\rho \times N_A \times n'}{M}$, where ρ is the density, N_A is Avogadro's constant, n' stands for the free electrons per atom, and M is the molar mass. The number density of charge carriers for an Au island is calculated to be $n = 5.8987 \times 10^{28}$ electrons m^{-3}. The radius of a Au island is $R_{Au} = 2.2\,\mu m$, while its thickness is 200 nm. The number of charge carriers is thus calculated as 1.7938×10^{11} electrons, where the electron charge is $e = 1.602 \times 10^{-19}$ C. The maximum electrical charge on the island is thus $Q_{max} = 2.8737 \times 10^{-8}$ C. Furthermore, the current density is $J = \sigma E$, where E represents the electric field inside the Au plate and σ denotes its conductivity ($\sigma = 4.10 \times 10^7$ S/m). Figure 5 shows a plot of the resistance of the gold plate as a function of its radius and thickness, revealing a decrease with increasing diameter or radius. In other words, the resistance of the Au plate to the flow of charges decreases as its thickness is increased.

Figure 6 shows plots of the current and voltage, where the current remains steady with an increase in the voltage

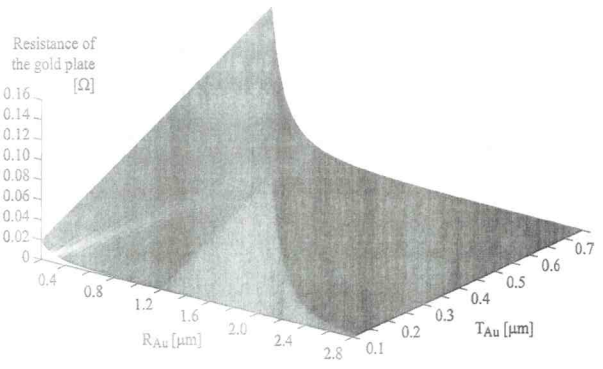

Fig. 5 The resistance of the gold plate as a function of the radius and thickness of the gold plate island

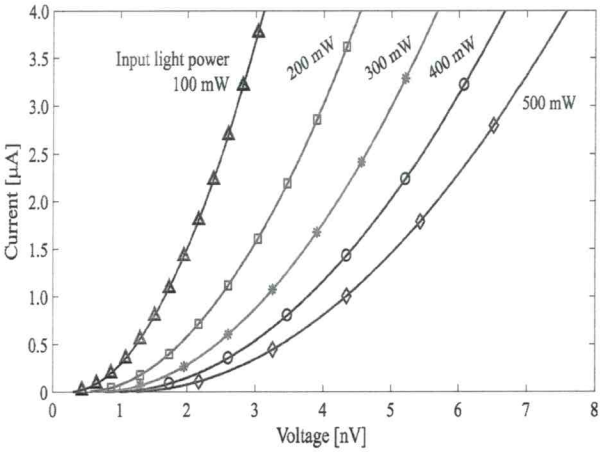

Fig. 6 A plot of the current within the gold plate island as a function of the voltage, where the input light power is varied from 100 to 500 mW, corresponding to sensitivity values of 1.96 μA nV^{-1}, 1.34 μA nV^{-1}, 1.13 μA nV^{-1}, 0.93 μA nV^{-1}, and 0.82 μA nV^{-1}, respectively

as the input light power is varied from 100 to 500 mW with an average sensitivity of 1.0 μA nV^{-1}. Such a current is known as the persistent current, remaining steady as the voltage increases and thus exhibiting the characteristic of a superconductor. The response of the microring circuit to an electric field can be described by London's equation $\frac{\partial J_s}{\partial t} = \frac{n_s e^2}{m} E$ [24], which describes how normal electrons are scattered, leading to a current. The electric field is constant if there is no scattering of electrons, with a steady increase in the current density in an electric field. When a constant current flows in a superconducting material, then $\frac{\partial J_s}{\partial t} = 0$ and $E = 0$, which implies that the resistance $R = \frac{V}{I}$ approaches zero as the electric field within the superconducting material approaches zero. Under space–time distortion control, the electric field passing through the microring circuit experiences a sudden collapse due to the Rabi oscillation, when the Rabi oscillation signal collapses [25]. This means that the transported polaritons are in the stopped state, as shown in Fig. 7. A plot of the effect of the collapse of the Rabi oscillation on the electric field is shown in Fig. 8, where the switching time is 1.50 μs. This phenomenon causes the microring-embedded gold-island device to become a superconducting sensing circuit that can be employed in superconducting circuit applications. According to Fig. 1, the space–time control is applied by multiplexing the space–time signals via the add port, where the first and second input signals from the input and add ports are multiplexed and propagate within the circuit. The optical path difference in space and time can be adjusted using the nonlinear Kerr effect, mainly being obtained from the two side rings. The resonance of the successive filtering (20,000 round trips) circuit is achieved when space and time uncertainty saturation is

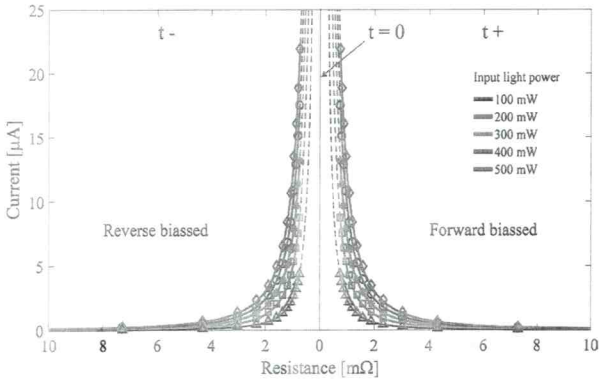

Fig. 7 The two sides of the temporal *I–R* curve, where the switching is the Rabi frequency oscillation [25]. The Rabi oscillation switching time is 1.50 μs

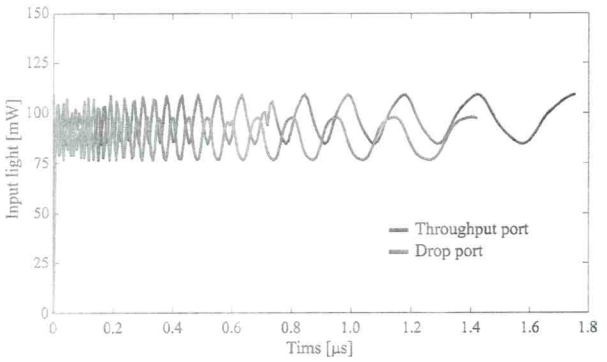

Fig. 8 A plot of the electric field intensity versus time when the electric field tends to zero as the Rabi oscillation frequency collapses; the switching of the drop and throughput port is achieved at 1.5 and 1.6 μs

established, where squeezed polaritons occur. The relationship of space and time is $E{\cdot}\Delta E \cdot \Delta t = \Delta z \cdot \Delta p{\sim}\hbar$, which saturates simultaneously. The particles (polaritons) propagating within the microring resonator can be described by a two-level system called the Rabi oscillation [25]. The two-level system oscillation collapses at the stopped state, where $t = 0$, in which case the circuit resistance approaches zero. Under space–time distortion control, the stopping state of the polaritons is established when the successive filtering is at resonance. This corresponds to space–time uncertainty saturation, where the space–time distortion vanishes. The particles (polaritons) propagate within the microring resonator and exhibit the Rabi oscillation, which is stopped at the uncertainty saturation. When the two-level system oscillation collapses at the stopped state, then $t = 0$, which in this case means that the circuit resistance approaches zero. As shown in Fig. 1b, the applied external environment in terms of a low current is coupled to the circuit island and flows in the circuit. The electron density output resulting from the changes can be detected at the drop port (Fig. 3a), while the space–time control is achieved via the add port (Fig. 1b). The throughput port is applied for transmission over a long-distance link. The sensing mechanism is manipulated by variation of the input power applied to the input port, for which the results are shown in Figs. 4, 5, and 6, which can be applied for either reverse- or forward-biased operation, as shown in Fig. 7 for the standby condition ($t = 0$). The switching condition of the Rabi oscillation between on and off is 1.4 and 1.8 μs, as shown in Fig. 6.

4 Conclusions

A microring circuit with an embedded gold island for use in superconducting sensors for low-current measurements is proposed. The input electric field illuminates a gold island film at the center, leading to the excitation of electrons, based on which the trapped electron densities can be transported via the soliton WGM. The space–time distortion controls the response of the microring circuit to the electric field oscillation, finally resulting in the resonant electric field. When using suitable parameter values, superconducting sensing occurs in the circuit when the Rabi oscillation frequency collapses, and the electric field becomes zero between the two bias directions. i.e., forward and reverse. The Rabi frequency oscillation switching time is 1.50 μs. The current and voltage characteristics of the circuit reveal sensitivity values ranging from 0.82 to 1.90 μA nV^{-1}. A circuit such as that proposed herein could be applied for low-current power transmission via either wireless or cable connections. In addition, various sensor configurations based on such low-current sensors could also be designed using the proposed space–time control circuit.

Acknowledgements The authors would like to acknowledge the research facilities from Rajamangala University of Technology Phra Nakhon, Bangkok, Thailand and Ton Duc Thang University, Vietnam, and the financial support from Rajamangala University of Technology Phra Nakhon, Bangkok, Thailand.

References

1. Zhiliche, Y.: Modeling of current density in cylindrical superconductors by separation of variables. IEEE Trans. Appl. Supercond. **29**(2), 1–4 (2020)
2. Sadleir, J.E., et al.: Magnetically tuned superconducting transition-edge sensors. IEEE Trans. Appl. Supercond. **23**(3), 1–5 (2013)
3. Chen, J.K., et al.: Full-chip thermal simulation of superconductor transition-edge sensor circuits. IEEE Trans. Appl. Supercond. **28**(1), 1–5 (2018)
4. Kvitkovic, J., et al.: Enhanced magnetic field sensing using planar high-temperature superconductor shields. IEEE Trans. Appl. Supercond. **28**(4), 1–5 (2018)

5. Wang, G., et al.: Modeling iridium-based trilayer and bilayer transition-edge sensors. IEEE Trans. Appl. Supercond. **27**(4), 1–5 (2017)
6. Kunniyoor, K.R., et al.: A mathematical model for the characterization of superconducting level sensors. IEEE Trans. Appl. Supercond. **28**(1), 1–11 (2018)
7. Wang, T.S., et al.: Device modeling of superconductor transition-edge sensors based on the two-fluid theory. IEEE Trans. Appl. Supercond. **22**(4), 1–12 (2012)
8. Holdengreber, E., et al.: Superior impedance matching of THz antennas with high temperature superconducting Josephson junctions. Supercond. Technol. **32**(7), 1–10 (2019)
9. Shibata, H., et al.: Photoresponse of $La_{1.85}Sr_{0.15}CuO_4$ nanostrip. Supercond. Sci. Technol. **30**(7), 1–9 (2017)
10. Sun, L., Cherpak, N., Barannik, A., He, Y.S., Glamazdin, V., Zhang, X., Wang, J., Zolotaryov, V.: New type of microwave high-Tc superconductor microstrip resonator and its application prospects. IEEE Trans. Appl. Supercond. 27(4), 1–5 (2017)
11. Kato, T., Saito, A., Tsurui, R., Teshima, H., Ohshima, S.: Power-handling capability of superconducting filters using disk- and ring-type bulk resonators. IEEE Trans. Appl. Supercond. **25**(3), 1–5 (2015)
12. Sekiya, N., Matsuura, H., Akiya, M., Tanaka, Y., Ohshima, S.: Novel HTS double-strip resonator for high power application. IEEE Trans. Appl. Supercond. **23**(3), 1–4 (2013)
13. Pi, W., Ou, Y., Wang, Y., Dong, J., Shi, X.: Numerical and experimental study on current distribution of LTS/HTS hybrid superconductor. IEEE Trans. Appl. Supercond. 26(4), 1–5 (2016)
14. Xiang, B., Liu, Z., Geng, Y., Yanabu, S.: DC circuit breaker using superconductor for current limiting. IEEE Trans. Appl. Supercond. **25**(2), 1–7 (2015)
15. Zhu, J., Zhang, Z., Zhang, H., Zhang, M., Qiu, M., Yuan, W.: Electric measurement of the critical current, AC loss, and current distribution of a prototype HTS cable. IEEE Trans. Appl. Supercond. **24**(3), 1–4 (2014)
16. Li, Z., Yang, Z., Xing, Y., Zhu, W., Su, J., Kong, X., Jiang, J., Du, B.: Improving the electric field distribution in stress cone of HTS dc cable terminals by nonlinear conductive epoxy/ZnO composites. IEEE Trans. Appl. Supercond. **29**(2), 1–4 (2019)
17. Khomyuth, C., Mahdi, B., Amiri, I.S., Youplao, P., Pornsuwancharoen, N., Yupapin, P.: Electric-optic conversion circuit incorporating a fiber optic loop for light fidelity up-down link use. Microw. Opt. Technol. Lett. **61**(2), 526–531 (2018)
18. Arumona, A.E., Amiri, I.S., Yupapin, P.: Plasmonic micro-antenna characteristics using gold grating embedded panda-ring circuit. Plasmonics **15**, 279–285 (2020)
19. Tunsiri, S., Thammawongsa, N., Threepak, T., Mitatha, S., Yupapin, P.: Microring switching control using plasmonic ring resonator circuits for super-channel use. Plasmonics **14**, 1669–1677 (2019)
20. Prateep, P., Surasak, C., Yupapin, P.: Analytical and simulation of a triple micro whispering gallery mode probe system for a 3D blood flow rate sensor. Appl. Opt. **65**, 9504–9513 (2016)
21. Kittel, C., Kroemer, H.: Thermal Physics, 2nd edn. W.H. Freeman, San Francisco (1980). ISBN 0-7167-1088-9
22. Yupapin, P., Teeka, C., Ali, J.: Nanoscale Nonlinear PANDA Ring Resonator, 1st edn. CRC Press, Boca Raton (2012)
23. OptiFDTD Technical Background and Tutorials (Finite Difference Time Domain) Photonics Simulation Software, Version 12.0. http://www.optiwave.com. Searched on 20th Sept 2019
24. Misra, P.K.: Physics of Condensed Matter, 1st edn, pp. 451–468. Academic, Cambridge (2012)
25. Arumona, A.E., Amiri, I.S., Yupapin, P.: Full-time slot teleportation using unified space-time function control. Microw. Opt. Technol. Lett. **14**(2019), 1–7 (2019)
26. Pornsuwancharoen, N., et al.: Micro-current source generated by a WGM of light within a stacked silicon-graphene-Au waveguide. IEEE Photon. Technol. Lett. **29**(21), 1768–1771 (2017)
27. Prabhu, A.M., Tsay, A., Han, Z., Van, V.: Extreme miniaturization of silicon add-drop microring filters for VLSI photonics applications. IEEE Photonics J. **2**(3), 436–444 (2010)

Journal of Computational Electronics

ISSN: 1569-8025
eISSN: 1572-8137
SPRINGER
ONE NEW YORK PLAZA, SUITE 4600 , NEW YORK, NY 10004, UNITED STATES
USA

Go to Journal Table of Contents Go to Ulrich's Printable Version

TITLES
ISO: J. Comput. Electron.
JCR Abbrev: J COMPUT ELECTRON

CATEGORIES
PHYSICS, APPLIED -- SCIE
ENGINEERING, ELECTRICAL & ELECTRONIC -- SCIE

LANGUAGES
English

PUBLICATION FREQUENCY
4 issues/year

The data in the two graphs below and in the Journal Impact Factor calculation panels represent citation activity in 2019 to items published in the journal in the prior two years. They detail the components of the Journal Impact Factor. Use the "All Years" tab to access key metrics and additional data for the current year and all pri years for this journal.

Journal Impact Factor Trend 2019

Printable Version

1.532
2019 Journal Impact Factor

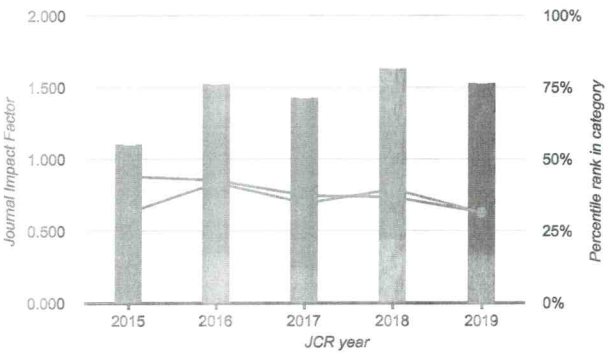

Citation distribution 2019

Printable Version

1 Article citation median **0** Review citation median

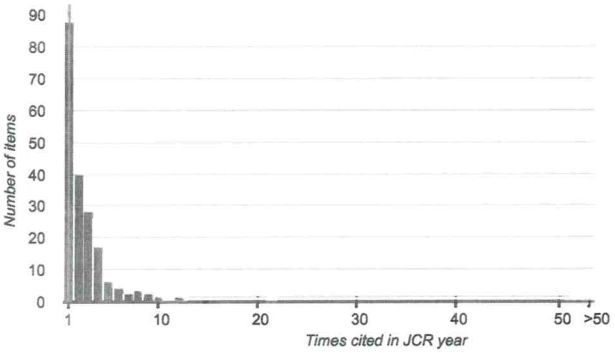

Journal Impact Factor Calculation

2019 Journal Impact Factor = 481 / 314 = 1.532

How is Journal Impact Factor Calculated?

$$JIF = \frac{\text{Citations in 2019 to items published in 2017 (230) + 2018 (251)}}{\text{Number of citable items in 2017 (124) + 2018 (190)}} = \frac{481}{314}$$

Journal Impact Factor contributing items

Show all

Citable items in 2018 and 2017 (314) Citations in 2019 (481)

TITLE	CITATIONS COUNTED TOWARDS JIF
: a physical model for RRAM devices simulation By: Villena, Marco A.; Roldan, Juan B.; Jimenez-Molinos, Francisco; Miranda, Enrique; Sune, Jordi et al. **Volume: 16 Page: 1095-1120 Accession number: WOS:000417598100012** **Document Type: Article**	12
Magnetic properties of bilayer graphene: a Monte Carlo study By: Masrour, R.; Jabar, A. **Volume: 16 Page: 12-17 Accession number: WOS:000394370700002** **Document Type: Article**	10
Heterogate junctionless tunnel field-effect transistor: future of low-power devices By: Rahi, Shiromani Balmukund; Asthana, Pranav; Gupta, Shoubhik **Volume: 16 Page: 30-38 Accession number: WOS:000394370700005** **Document Type: Article**	9
Performance analysis and enhancement of 10-nm GAA CNTFET-based circuits in the presence of CNT-metal contact resistance By: Moaiyeri, Mohammad Hossein; Razi, Farzad Volume: 16 Page: 240-252 Accession number: WOS:000400106400003	9

Document Type: Article	
Boosting the performance of a nanoscale graphene nanoribbon field-effect transistor using graded gate engineering By: Tamersit, Khalil; Djeffal, Faycal **Volume: 17 Page: 1276-1284 Accession number: WOS:000442609200041** **Document Type: Article**	8
Tuning electronic, magnetic, and transport properties of blue phosphorene by substitutional doping: a first-principles study By: Safari, Fatemeh; Fathipour, Morteza; Goharrizi, Arash Yazdanpanah **Volume: 17 Page: 499-513 Accession number: WOS:000431208600002** **Document Type: Article**	8
Memory selector devices and crossbar array design: a modeling-based assessment By: Chen, An **Volume: 16 Page: 1186-1200 Accession number: WOS:000417598100018** **Document Type: Article**	8

Source data | Box plot | Rank | Cited Journal Data | Citing Journal Data | Journal Relationships

Journal source data 2019

	Articles	Reviews	Combined(C)	Other(O)	Percentage(C/(C+O))
Number in JCR Year 2019 (A)	145	1	146	1	99%
Number of References (B)	4,835	75	4,910	1	100%
Ratio (B/A)	33.3	75.0	33.6	1.0	

Key Indicators 2019

IMPACT METRICS

Total Cites	1,433	✓Trend
Journal Impact Factor	1.532	Trend
5 Year Impact Factor	1.473	Trend
Immediacy Index	0.404	Trend
Impact Factor without Journal Self Cites	1.382	Trend

INFLUENCE METRICS

Eigenfactor Score	0.00235	Trend
Article Influence Score	0.269	Trend
Normalized Eigenfactor	0.28710	Trend

SOURCE METRICS

Citable Items	146	Trend
% Articles in Citable Items	99.32	Trend
Average JIF Percentile	31.442	Trend
Cited Half-Life	3.7	Trend
Citing Half-Life	8.4	Trend

Metric Trend Total Cites

Export

View All Years

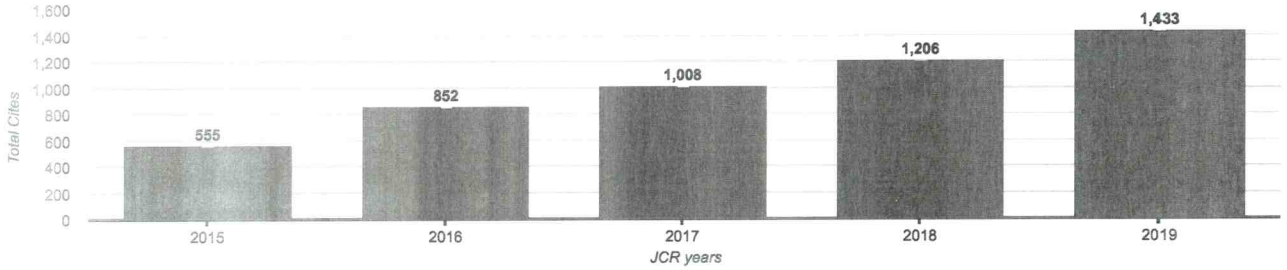

Journal profile [2017 - 2019]

Open Access (OA)

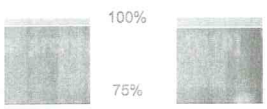

Contributions by country/region

	country	count
1	India	164

Contributions by organizations

	organization	count
1	ISLAMIC AZAD UNIVERSITY	21

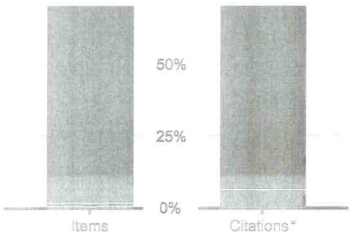

	Items	Citations*
Gold OA Citable	11	18
Subscription and Free to Read Citable	449	490
Total Citable	460	508
% Citable Open Access	2.39%	3.54%
Other	4	0
Unlinked	n/a	32

*Citations in 2019 to items published in [2017 - 2019]

2	Iran	64
3	CHINA MAINLAND	49
4	USA	45
5	Algeria	35
6	Saudi Arabia	16
7	Italy	11
8	GERMANY (FED REP GER)	10
-	South Korea	10
-	Tunisia	10

2	INDIAN INSTITUTE OF TECHNOLOGY SYSTEM (IIT SYSTEM)	20
3	VELLORE INSTITUTE OF TECHNOLOGY	14
4	SHAHID BEHESHTI UNIVERSITY	13
5	JADAVPUR UNIVERSITY	8
-	NATIONAL INSTITUTE OF TECHNOLOGY DURGAPUR	8
-	NATIONAL INSTITUTE OF TECHNOLOGY SILCHAR	8
-	SHANMUGHA ARTS, SCIENCE, TECHNOLOGY & RESEARCH ACADEMY (SASTRA)	8
9	ARIZONA STATE UNIVERSITY	7
-	DR TAHAR MOULAY UNIV SAIDA	7
-	INDIAN INSTITUTE OF INFORMATION TECHNOLOGY DESIGN & MANUFACTURING, JABALPUR	7
-	SEMNAN UNIVERSITY	7

Journal of Computational Electronics

Editorial board Aims & scope Journal updates

The Journal of Computational Electronics brings together research on all aspects of modeling and simulation of modern electronics. This includes optical, electronic, mechanical, and quantum mechanical aspects, as well as research on the underlying mathematical algorithms and computational details. The related areas of energy conversion/storage and of molecular and biological systems, in which the thrust is on the charge transport, electronic, mechanical, and optical properties, are also covered.

In particular, we encourage manuscripts dealing with device simulation; with optical and optoelectronic systems and photonics; with energy storage (e.g. batteries, fuel cells) and harvesting (e.g. photovoltaic), with simulation of circuits, VLSI layout, logic and architecture (based on, for example, CMOS devices, quantum-cellular automata, QBITs, or single-electron transistors); with electromagnetic simulations (such as microwave electronics and components); or with molecular and biological systems. However, in all these cases, *the submitted manuscripts should explicitly address the electronic properties of the relevant systems, materials, or devices and/or present novel contributions to the physical models, computational strategies, or numerical algorithms.*

The Editors will emphasize advances and challenges arising from applications in multiscale problems focusing on those whose basis arises from physical and chemical sciences. A short list of the specific topics that lie within the scope of this new journal is as follows:

- Semiconductor Devices
- Optical Devices, Plasmonics, and Photonics
- Process Simulation
- Energy and Environment

- Nano-electro-mechanical systems
- Mathematical Approaches
- Open Quantum Systems

- Examines the full spectrum of modeling and simulation of modern electronics
- Addresses optical, electronic, mechanical, and quantum mechanical aspects of the field
- Investigates underlying mathematical algorithms and computational details
- Draws special attention to the advances and challenges arising from applications in multiscale problems

---

Editors-in-Chief

Massimo V. Fischetti, Stephen Goodnick

Publishing model

Hybrid. Open Access options available

1.532 (2019)

Impact factor

1.473 (2019)

Five year impact factor

53 days

Submission to first decision

186 days

Submission to acceptance

75,038 (2019)

Downloads

Latest issue

Volume 19

Issue 3, September 2020